

VRIJE  
UNIVERSITEIT  
BRUSSEL

<sup>1</sup> **A search for flavour changing neutral currents  
2 involving a top quark and a Z boson, using the  
3 data collected by the CMS collaboration at a  
4 centre of mass of 13 TeV**

<sup>5</sup> Van Parijs, Isis

<sup>6</sup> Proefschrift ingediend met het oog op het behalen van de academische graad  
<sup>7</sup> Doctor in de Wetenschappen.

Published in Faculteit Wetenschappen & Bio-ingenieurswetenschappen  
Vrije Universiteit Brussel  
At 1. June 2017.

<sup>8</sup>

Responsible Contact: I. Van Parijs  
Institute for High Energy Physics  
Promotor: Prof. Jorgen D'Hondt

9      First Referee: Prof. Dr. J. D'Hondt  
      Date of Hand-in: 1 June 2017  
      Date of Defense: 1 October 2017

# Contents

---

|    |  |    |
|----|--|----|
| 11 | <b>1 An introduction to the theory</b>                                 | 1  |
| 12 | 1.1 Elementary particles and forces . . . . .                          | 1  |
| 13 | 1.2 Standard Model Lagrangian . . . . .                                | 1  |
| 14 | 1.3 Physics beyond the standard model . . . . .                        | 1  |
| 15 | 1.3.1 Effective field theory . . . . .                                 | 1  |
| 16 | 1.3.2 Motivations for new physics . . . . .                            | 1  |
| 17 | 1.3.3 Searches beyond the Standard Model . . . . .                     | 1  |
| 18 | 1.3.4 Experimental and theoretical constraints . . . . .               | 1  |
| 19 | 1.4 Statistics for a high energy particle physicist . . . . .          | 1  |
| 20 | 1.4.1 Boosted decision trees . . . . .                                 | 1  |
| 21 | 1.4.2 Confidence levels . . . . .                                      | 1  |
| 22 | 1.4.3 Combine limit setting tool . . . . .                             | 1  |
| 23 | <b>2 Experimental setup</b>  | 3  |
| 24 | 2.1 The Large Hadron Collider . . . . .                                | 3  |
| 25 | 2.1.1 LHC design and operation . . . . .                               | 5  |
| 26 | 2.2 The Compact Muon Solenoid . . . . .                                | 7  |
| 27 | 2.2.1 CMS coordinate system . . . . .                                  | 8  |
| 28 | 2.2.2 Towards the heart of CMS . . . . .                               | 9  |
| 29 | 2.2.3 Data acquisition . . . . .                                       | 18 |
| 30 | 2.2.4 CMS computing model . . . . .                                    | 18 |
| 31 | <b>3 Event generation, simulation and reconstruction</b>               | 21 |
| 32 | 3.1 Collision event generation . . . . .                               | 21 |
| 33 | 3.1.1 Parton distribution functions and the hard interaction . . . . . | 21 |
| 34 | 3.1.2 Parton showering . . . . .                                       | 21 |
| 35 | 3.1.3 Hadronization and decay . . . . .                                | 21 |
| 36 | 3.1.4 Underlying event . . . . .                                       | 21 |
| 37 | 3.1.5 Event reconstruction and identification . . . . .                | 21 |
| 38 | 3.2 Detector simulation . . . . .                                      | 21 |
| 39 | 3.3 Physics object reconstruction and identification . . . . .         | 21 |
| 40 | 3.3.1 The particle flow event reconstruction method . . . . .          | 21 |
| 41 | 3.3.2 Identification of particles . . . . .                            | 21 |

|    |  |           |
|----|--|-----------|
| 42 | 3.3.3 Calibrations and corrections . . . . .                     | 21        |
| 43 | <b>4 The search for FCNC involving a top quark and a Z boson</b> | <b>23</b> |
| 44 | 4.1 Model assumptions . . . . .                                  | 23        |
| 45 | 4.2 Data and simulation . . . . .                                | 23        |
| 46 | 4.2.1 Standard Model Background simulation . . . . .             | 23        |
| 47 | 4.2.2 FCNC signal simulation . . . . .                           | 23        |
| 48 | 4.2.3 Trigger requirements . . . . .                             | 23        |
| 49 | 4.3 Baseline event selection . . . . .                           | 23        |
| 50 | 4.4 Data driven background estimation . . . . .                  | 23        |
| 51 | 4.5 Regions and channels . . . . .                               | 23        |
| 52 | 4.6 Construction of template distributions . . . . .             | 23        |
| 53 | 4.7 Systematic uncertainties . . . . .                           | 23        |
| 54 | 4.8 Limit setting procedure . . . . .                            | 23        |
| 55 | 4.9 Result and discussion . . . . .                              | 23        |
| 56 | <b>5 Conclusion and outlook</b>                                  | <b>25</b> |
| 57 | <b>Bibliography</b>  | <b>27</b> |

# Theoretical bases

1

---

59 **1.1 Elementary particles and forces**

60 **1.2 Standard Model Lagrangian**

61 **1.3 Physics beyond the standard model**

62 **1.3.1 Effective field theory**

63 **1.3.2 Motivations for new physics**

64 **1.3.3 Searches beyond the Standard Model**

65 **1.3.4 Experimental and theoretical constraints**

66 **1.4 Statistics for a high energy particle physiscist**

67 **1.4.1 Boosted decision trees**

68 **1.4.2 Confidence levels**

69 **1.4.3 Combine limit setting tool**



# Experimental setup

# 2

---

71 The main objective of the Large Hadron Collider (LHC) was the search for the Brout-Englert-  
 72 Higgs boson (or scalar boson). It was known from the Linear Electron Positron(LEP)[Myers:226776]■  
 73 and Tevatron[1748-0221-6-08-T08001] experiments that the scalar boson mass had to be  
 74 larger than 114 GeV[1, 2], and smaller than around 1 TeV due to unitarity and perturbativity  
 75 constraints [3]. On top of this, the search of supersymmetry or dark matter were part of the mo-  
 76 tivation for building the LHC. Since the start of its operation, the LHC is pushing the boundaries  
 77 of the Standard Model, putting the best limits on physics beyond the Standard Model as well as  
 78 precision measurements of the parameters of the Standard Model. One such an accomplishment  
 79 is the discovery the scalar boson in 2012 by the two largest experiments at the LHC [4, 5].

80 In the first part of this chapter, the LHC and the acceleration process for protons to reach  
 81 their design energies is discussed. The second part presents the Compact Muon Solenoid.

## 82 2.1 The Large Hadron Collider

83 The LHC has started its era of cutting edge science on 10 September 2008 [6] after approval by  
 84 the European Organisation of Nuclear Research (CERN) in 1995 [7]. Installed in the previous  
 85 Large Electron Positron collider (LEP) tunnels, the LHC consists of a 26.7 km ring, that is  
 86 installed between 45 and 170 m under the French-Swiss border between Cessy (France) and  
 87 Meyrin (Switzerland). Built to study rare physics phenomena at high energies, the LHC has the  
 88 possibility to accelerate two type of particles - protons or ions  $Pb^{45+}$  - and provides collisions  
 89 at four points of interaction or bunch crossings.. At the interaction points, experiments are  
 90 installed in order to study the collisions.

91 As can be seen in [Figure 2.1](#), the LHC is last element in a chain of creation, injection and  
 92 acceleration of protons. Protons are obtained by ionising hydrogen and injected in a linear  
 93 accelerator (LINAC 2), where they obtain an energy of 50 MeV. They continue to the proton  
 94 synchrotron booster (PSB or Booster), where the proton packets are accelerated to 1.4 GeV and  
 95 are split up in twelve. The proton synchrotron (PS) increases their energy to 25 GeV before  
 96 handing the protons to the super proton synchrotron (SPS), where the proton reach an energy  
 97 of 450 GeV. Each accelerator ring increases in radius in order to reduce the energy loss of the  
 98 protons by synchrotron radiation. This energy loss is proportional to the fourth power of the

proton energy and inversely proportional to the bending radius. The protons are then injected into opposite directions into the LHC, where they are accelerated to 3.5 TeV (in 2010 and 2011), 4 TeV (in 2012 and 2013) or 6.5 TeV (in 2015 and 2016) [8]. Before the start up of the LHC in 2010, the previous energy record was held by the Tevatron collider at Fermilab, colliding proton with antiprotons at  $\sqrt{s} = 1.96$  TeV.

The beam has a bunch structure obtained by the injection scheme and properties of the dump system. These bunches are obtained in the PS with 25 ns spacing for run II. The operation of accelerating and transferring to the LHC is repeated 12 times for each counter-rotating beam. When completely filled, the LHC nominally contains 2220 bunches in run II, compared to 1380 in run I (design: 2200). At full intensity, it would have nearly 2800 bunches but this is limited due to SPS.

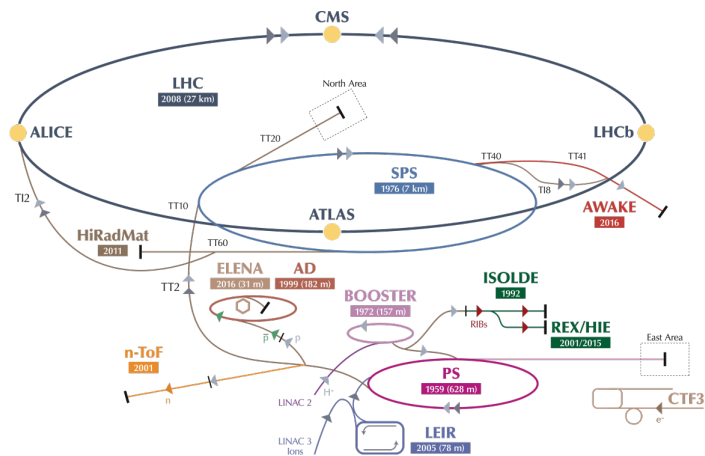


**Figure 2.1:** Schematic representation of the accelerator complex at CERN [9]. The LHC (dark blue) is the last element in chain of accelerators. Protons are successively accelerated by LINAC 2, the Booster, the Proton Synchrotron (PS) and the Super Proton Synchrotron (SPS) before entering the LHC.

The LHC is home to seven experiments that are placed on an interaction point:

- A Toroidal LHC ApparatuS (ATLAS [10]) and the Compact Muon Solenoid (CMS [11]) experiments are the two general purpose detectors at the LHC. They both have a hermetic, cylindrical structure and were designed to search for new physics phenomena as well as precision measurements of the Standard Model. The existence of two distinct experiments allows cross-confirmation for any discovery.
  - A Large Ion Collider Experiment (ALICE [12]) and the LHC Beauty (LHCb [13]) experiments are focusing on specific phenomena. ALICE studies strongly interacting matter at extreme energy densities where quark-gluon plasma forms from heavy ions (Pb-Pb or p-Pb). LHCb searches for differences between matter and anti matter by means of the b quark, while focussing on CP symmetry violation.
  - The forward LHC (LHCf [14]) and the TOTal cross section, Elastic scattering and diffraction dissociation Measurement (TOTEM [15]) experiments are two smaller experiments that

123 focus on interactions where protons or heavy ions only meet while head on collisions take  
 124 place. LHCf consists of two parts placed before and after ATLAS and studies particles  
 125 created at very small angles. TOTEM is placed in the same cavern as CMS and performs  
 126 precise measurements of the LHC luminosity.

- 127 • The Monopoles and Exotics Detector At the LHC (MoEDAL [16]) experiment is situated  
 128 near LHCb and tries to find magnetic monopoles.

129 **2.1.1 LHC design and operation**

The most important quantity at the LHC is the luminosity[17]. This is a measurement of the number of collisions that can be produced in a detector per  $\text{m}^2$  and per second. The LHC collisions create a number of events per second given by

$$N_{\text{event}} = L\sigma_{\text{event}}, \quad (2.1)$$

where  $\sigma_{\text{event}}$  is the cross section of the event of interest and  $L$  the machine luminosity. This luminosity depends only on the beam parameters and is for a Gaussian beam expressed as

$$L = \frac{1}{4\pi} \textcolor{blue}{N_b} n_b f_{\text{rev}} \frac{\textcolor{red}{N_b}}{\epsilon_n} \left( 1 + \left( \frac{\theta_c \sigma_z}{2\sigma^*} \right)^2 \right)^{-\frac{1}{2}} \frac{\gamma_r}{\beta^*}. \quad (2.2)$$

130 The number of particles per bunch is expressed by  $N_b$ , while  $n_b$  is the number of bunches  
 131 per beam,  $f_{\text{rev}}$  the revolution frequency,  $\gamma_r$  the relativistic gamma factor,  $\epsilon_n$  the normalized  
 132 transverse beam emittance - a quality for the confinement of the beam ,  $\beta^*$  the beta function at  
 133 the collision point - a measurement for the width of the beam,  $\theta_c$  the angle between the two  
 134 beams at the interaction point,  $\sigma_z$  the mean lengths of one packet, and  $\sigma^*$  the mean height of  
 135 one packet. In Equation 2.2), the blue part represents the stream of particles, the red represents  
 136 the brilliance; and the green part represents the geometric reduction factor due to the crossing  
 137 angle at the interaction point. Hence, in order to enhance the chances for exploration of rare  
 138 events and thus enhancing the number of collisions. High beam energies as well as high beam  
 139 intensities are required.

140 The peak design luminosity for the LHC in 2016 was  $10^{34} \text{ 1}/(\text{m}^2 \text{ s})$ , which leads to about 1  
 141 billion proton interactions per second. In 2016, the LHC was around 10% above this design  
 142 luminosity[18]. This luminosity is not a constant in time. It diminishes due to collisions between  
 143 the beams, and the interaction of the protons and the particle gas that is trapped in the centre  
 144 of the vacuum tubes due to the magnetic field. The intern diffusion of the beam degrades the  
 145 emittance and therefore also the luminosity. For this reason, the mean lifetime of a beam inside  
 146 the LHC is around 15 h. The integrated luminosity - the luminosity provided for a certain time  
 147 range - recorded by CMS and ATLAS over the year 2016 is given in Figure 2.1.1. In Run II, the  
 148 peak luminosity is  $13\text{-}17 \cdot 10^{33} \text{ 1}/(\text{cm}^2 \text{ s})$  compared to  $7.7 \cdot 10^{33} \text{ 1}/(\text{cm}^2 \text{ s})$  in Run I.

149 Inside the LHC ring [19], the protons are accelerated by the means of radio frequency cavities,  
 150 while 1232 magnets of approximately 15 m long, weighing 35 t ensure the deflection of the  
 151 beams. The cross section view of such a dipole is given in Figure 2.4. The two proton beams  
 152 circulate in opposite direction in separate pipes inside of the magnet. Through the use of a strong

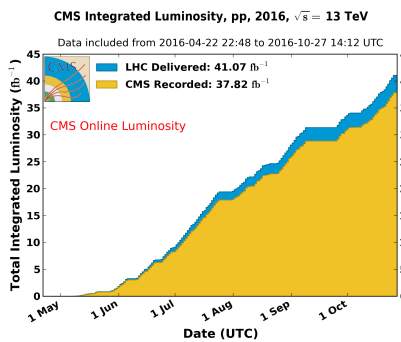


**Figure 2.2:** Cumulative luminosity measured online versus day delivered to (blue), and recorded by CMS (orange) during stable beams and for proton collisions at 13 TeV centre-of-mass energy in 2016. The delivered luminosity accounts for the luminosity delivered from the start of stable beams until the LHC requests CMS to turn off the sensitive detectors to allow a beam dump or beam studies.

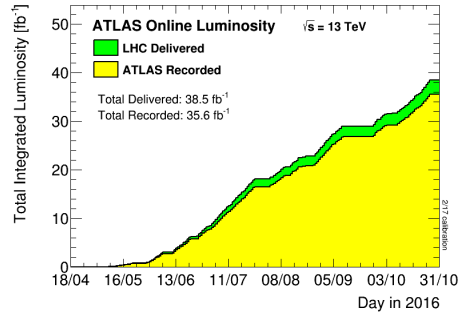


**Figure 2.3:** Total Integrated Luminosity in 2016 Cumulative luminosity versus time delivered to (green) and recorded by ATLAS (yellow) during stable beams for proton collisions in 2016. The delivered luminosity accounts for the luminosity delivered from the start of stable beams until the LHC requests ATLAS to put the detector in a safe standby mode to allow for a beam dump or beam studies. Shown is the luminosity as determined from counting rates measured by the luminosity detectors. )

153 electric current in the coils around the beam pipe, magnetic fields are generated and cause  
 154 the protons to bend in the required orbits. In order to get the coil to become superconducting  
 155 and able to produce - with the aid of an iron return yoke - a strong magnetic field of 3.8 T, the  
 156 magnet structure is surrounded by a vessel. This vessel is filled with liquid Helium making it  
 157 possible to cool down the magnet to 1.9 K. In order to get more focussed and stabilised proton  
 158 beam, other higher-order multipole and corrector magnets are placed along the LHC tunnel.

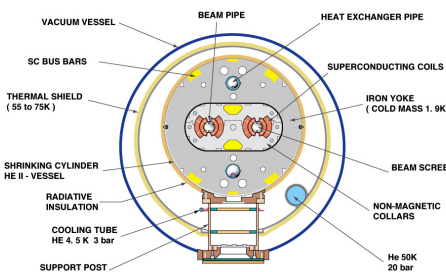


**Figure 2.4:** Schematic representation of the LHC dipole [20]. Two beam pipes where the proton beams circulate around the LHC ring are shown. The superconducting coils generate a magnetic field of 3.8 T that steer the protons in the circular path.

159 **2.2 The Compact Muon Solenoid**

160 At one of the collision points of the LHC, the CMS detector[21–23] is placed. Weighing 14 000  
 161 t, This cylindrical detector is about 28.7 m long and 15 m in diameter, weighing around 14 000  
 162 t. It has an onion like structure of several specialised detectors and contains a superconducting  
 163 solenoid with a magnetic field of 3.8 T. The CMS detector is designed in a way that it can  
 164 address the needs of physics coming from the LHC. Living in a hadronic environment, multi-jet  
 165 processes produced by the strong interaction are a main source of background for rare physics  
 166 processes. Therefore, good identification, momentum resolution, and charge determination of  
 167 muon, electrons and photons is one of the main goals of the CMS detector. Further it provides a  
 168 good charged particle momentum resolution and reconstruction efficiency in the inner tracker  
 169 such that for example jets coming from b quarks or tau particles can be identified. Also the  
 170 electromagnetic resolution for an efficient photon and lepton isolation as well as a good hadronic  
 171 calorimeter for the missing transverse energy were kept into account while designing CMS. In  
 172 [Figure 2.5](#), an overview of the CMS detector is given.

173 The LHC provides many collisions in a short amount of time. In order to discriminate between  
 174 consecutive collisions - known as out of time pile up events - , CMS has to complete the full data  
 175 acquisition for one collision event before the next one happens (around 25 ns in Run II and  
 176 around 50 ns in Run I [24]). Furthermore, since the photons are in packets, around 21 in Run  
 177 I and approximately 40 in Run II inelastic collisions happen every beam crossing . This creates  
 178 a great amount of background processes in the detector called in time pile up events. Due to  
 179 this difficult conditions, the detector has a high granularity which on its turn creates a need for  
 180 huge number of synchronized electronic channels. Furthermore, due to to high flux of particles  
 181 in the regions close to the beam, the electronics have to be able to endure high radiation.

182 Before the start of taking collision data for 13 TeV operations on 3 June, CMS had a long  
 183 shutdown (LS1)[26]. During this shut down several upgrades were performed. The innermost  
 184 part of detection material in CMS (pixel) is made of three concentric cylindrical layers in  
 185 run I. At the end of 2016 it is upgraded by adding a fourth layer, enhancing the particle  
 186 tracking capabilities of CMS. In order to be able to incorporate this new layer, the section  
 187 of the beryllium beam pipe within CMS was replaced by a narrower one during LS1. For  
 188 this, the pixel was removed and reinserted into CMS. In order to avoid long damage caused  
 189 by the intense particle flux at the heart of CMS, the tracker is been made ready to operate  
 190 at much lower temperature than before. During Run I, a small problem was detected in the  
 191 electromagnetic calorimeter preshower system. For this, the preshower discs were removed,  
 192 repaired and reinstalled successfully inside CMS in 2014. To help the discrimination between  
 193 interesting low momentum muons coming from collisions and muons caused by backgrounds, a  
 194 fourth triggering and measurement station for muons was added in each of the end caps. CMS  
 195 measures the collision rate within the detector and monitors beam related backgrounds. For  
 196 this, several new detectors were installed into CMS during LS1.

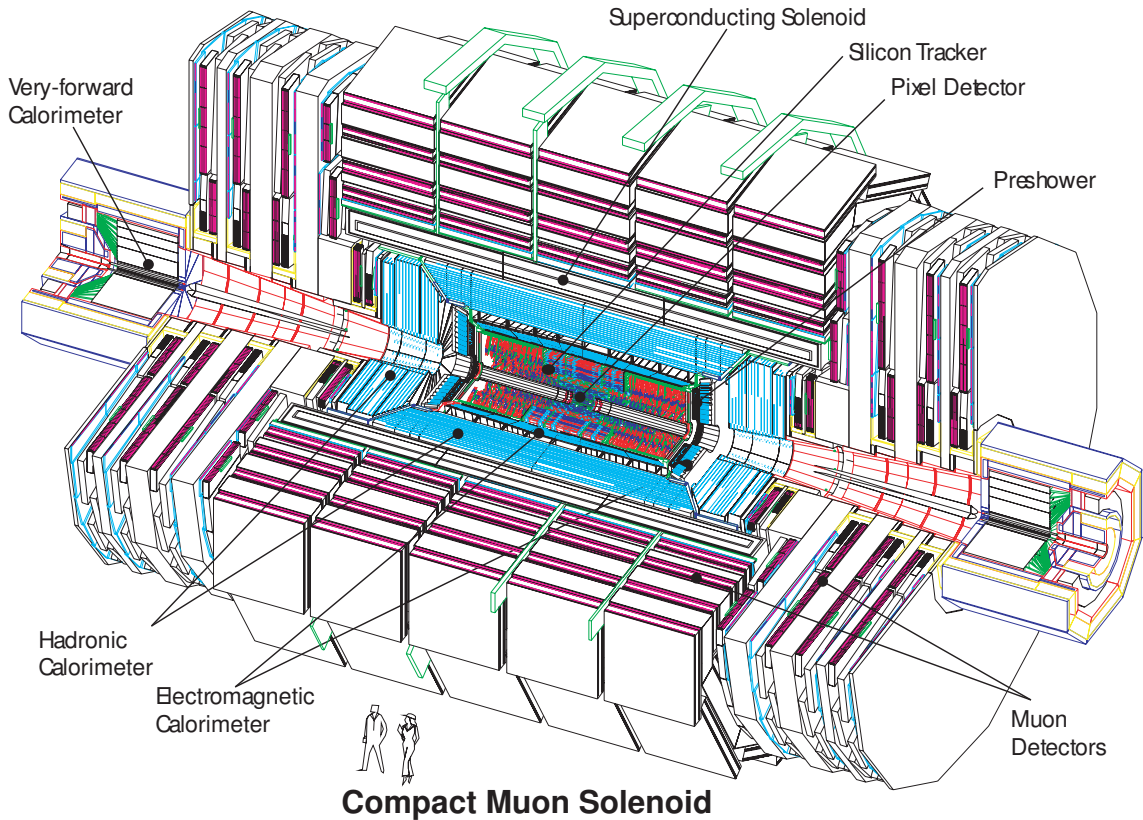


**Figure 2.5:** Mechanical layout of the CMS detector[25].

### 197 2.2.1 CMS coordinate system

The coordinate system used by CMS can be found in [Figure 2.6](#). The origin of the right handed orthogonal coordinate system is chosen to be the point of collisions. The x-axis points towards the centre of the LHC ring such that the y-axis points towards the sky, and the z-axis lies tangent to the beam axis. Since the experiment has a cylindrical shape, customary coordinates are used to describe the momentum  $\vec{p}$  : the distance  $\rho$ , the azimuthal angle  $\phi \in [-\pi, \pi]$  - the angle between the x-axis and the projection in the transverse plane of  $\vec{p}$  ( $p_T$ ) - , the pseudo-rapidity  $\eta$  - expressed by the polar angle  $\theta$  between the direction of  $\vec{p}$  and the beam - :

$$\eta = -\ln\left(\tan\left(\frac{\theta}{2}\right)\right). \quad (2.3)$$

For the energies considered at the LHC, where  $E \gg m$ , the pseudo-rapidity is a good approximation of the rapidity  $y$

$$y = \frac{1}{2} \ln\left(\frac{E + p_z}{E - p_z}\right), \quad (2.4)$$

198 where the difference of rapidities of two particles is invariant under a Lorentz boost in the  
199 z-direction.

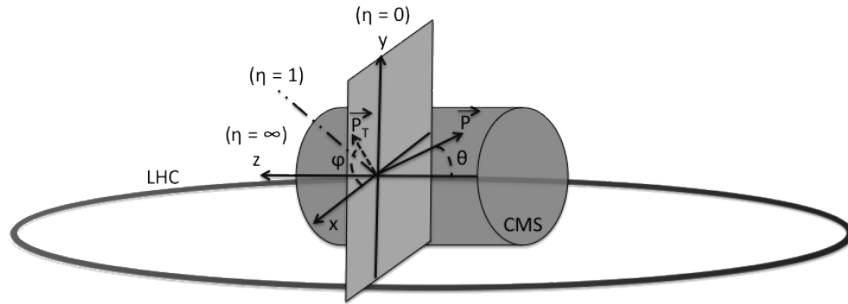


**Figure 2.6:** Representation of the coordinate system used by CMS. The point of origin is put at the collision point. The x-axis points towards the centre of the LHC ring such that the z-axis lies tangent to the beam axis.

### 2.2.2 Towards the heart of CMS

The CMS detector consists of two parts; a central barrel around the beam pipe ( $|\eta| < 1.4$ ) and two plugs to ensure the hermeticity of the detector. In Figure 2.5 and Figure 2.7 the onion like structure of the CMS detector is visible. The choice of a solenoid of 12.9 m long and 5.9 m diameter gives the advantage of bending the particle trajectories in the transverse plane. The hadronic calorimeter, the electromagnetic calorimeter and the tracker are within the solenoid, while the muon chambers are placed outside the solenoid.

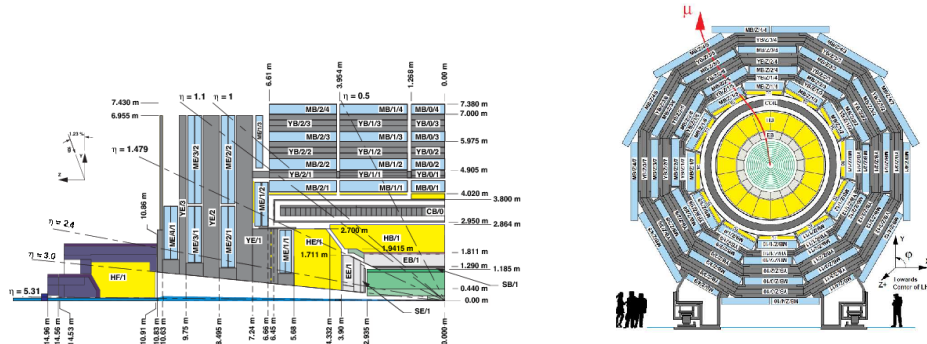


**Figure 2.7:** Schematic view of the CMS detector in the Run I configuration. (LEFT) Longitudinal view of one quarter of the detector. (RIGHT) Transversal view of one quarter of the detector. The muon system barrel elements are denoted as  $MBZ/N/S$ , where  $z = -2 \dots +2$  is the barrel wheel number,  $n = 1 \dots 4$  the station number and  $S = 1 \dots 12$  the sector number. Similarly, the steel return yokes are denoted as  $YBZ/N/S$ . The solenoid is denoted as  $CB0$ , while the hadronic calorimeter is denoted as  $HE$  (end cap)/ $HB$  (barrel)/ $HF$  (forward) and the electromagnetic calorimeter as  $EE$  (end cap)/ $EB$  (barrel). The green part represents the tracking system[27]

#### 2.2.2.1 Muon system

The outermost part of CMS consists of the muon system. The magnet return yoke is interleaved with gaseous detector chambers for muon identification and momentum measurement. The barrel contains muon stations arranged in five separate iron wheels, while in the end cap four

muon stations are mounted onto three independent iron discs on each side. Each barrel wheel has 12 sectors in the azimuthal angle.

The muon system is divided into three parts, shown in Figure 2.8[27]. The muon rate and neutron induced backgrounds are small and the magnetic field is very low for the barrel, thus CMS can use drift tube (DT) chambers. For the end caps however, the muon and background flux is much higher and there is a need to use cathode strip chambers (CSC) which are able to provide a faster response, higher granularity and have a better resistance against radiation. In order to form a redundant trigger system, resistive plate chambers (RPC) are added. This makes a total of 250 DT chambers, 540 CSC and 610 RPC. In Figure 2.7 the arrangement is shown.

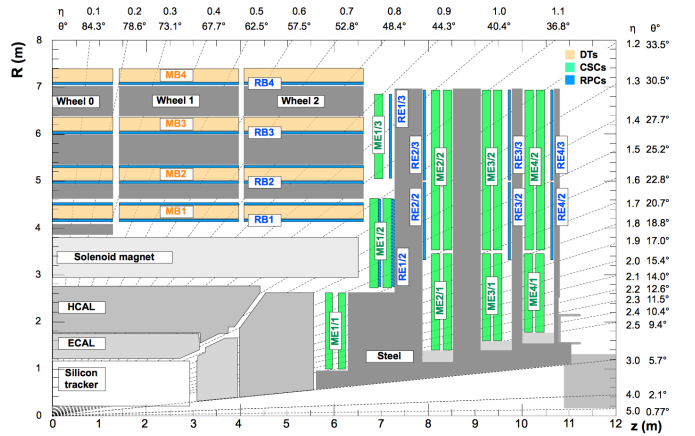


**Figure 2.8:** Schematic view of one quarter of the CMS muon system in the Run I configuration. [27]

Providing a measurement for  $|\eta| < 1.2$ . The DT chambers in the barrel are on average  $2 \times 2.5$  m in size and consist of 12 layers of DT cells - 4 cm wide gas tubes with positively charged stretched wire inside - arranged in three groups of four. The  $r\phi$  coordinate is provided by the two outside groups, while the middle group measures the  $z$  coordinate. For each  $\phi$  sector, the DT chamber is mixed with the flux return yoke. For the outer muon station, the DT chamber contains only 8 layers of DT cells, providing a muon position in the  $r\phi$  plane. There are four CSC stations in each end cap, providing muon measurements for  $0.9 < |\eta| < 2.4$  (Run I configuration). These CSC are multi-wired proportional chambers that consist of 6 anode wire planes crossed by 7 copper strips cathode panels in a gas volume. The  $r$  coordinate is provided by the copper strips, while  $\phi$  coordinate comes from the anode wires, giving a two dimensional position measurement. There are six layers of RPC in the barrel muon system and one layer into each of the first three stations of the end cap. They are made from two high resistive plastic plates with an applied voltage and separated by a gas volume. Read out strips mounted on top of the plastic plates detect the signal generated by a muon passing through the gas volume. The RPC provides a fast response with a time resolution of 1 ns and covers a range of  $|\eta| < 1.8$  (Run I configuration).

During the LS1, the muon system underwent major upgrades [28, 29]. In the fourth station of each end cap, the outermost rings of CSC and RPC chambers were completed, providing an

239 angular region of  $1.2 < |\eta| < 1.8$  for Run II, increasing the system redundancy, and allowing  
 240 tighter cuts on the trigger quality. In order to reduce the environmental noise, outer yoke discs  
 241 have been placed on both sides for the end caps. At the innermost rings of the first station, the  
 242 CSC has been upgraded by refurbishing the readout electronics to make use of the full detector  
 243 granularity instead of groups of three (Run I).

244 The muon system provides triggering on muons, identifying muons and improves the momentum  
 245 measurement and charge determination of high  $p_T$  muons. On top of the muon system,  
 246 the muon energy is deposited in the electromagnetic calorimeter, the hadronic calorimeter, and  
 247 outer calorimeter. The high magnetic field enables an efficient first level trigger and allows a  
 248 good momentum resolution of  $\Delta p/p \approx 1\%$  for a  $p_T$  of 100 GeV and  $\approx 10\%$  for a  $p_T$  of 1 TeV  
 249 (FIXME). There is an efficient muon measurement up to  $|\eta| < 2.4$ .

## 250 Muon reconstruction

251 The muon reconstruction[30] has three subdivision: local reconstruction, regional reconstruction  
 252 and global reconstruction. The local reconstruction is performed on individual detector elements  
 253 such as strip and pixel hits in the inner tracking system, and muon hits and/or segments  
 254 on the muon chambers. Independent tracks are reconstructed in the inner tracker - called  
 255 tracker track - and in the muon system, called standalone tracks. Based on these tracks,  
 256 two reconstructions are considered. The outside-in approach is referred to as Global Muon  
 257 reconstruction. For each standalone track, a tracker track is found by comparing the parameters  
 258 of the two tracks propagated onto a common surface. Combining the hits from the tracker  
 259 track and the standalone track, gives a fit via the Kalman filter technique [31, 32] for a global  
 260 muon track. The second approach is an inside-out reconstruction, creating tracker muons. All  
 261 candidate tracker tracks are extrapolated to the muon system taking into account the magnetic  
 262 field, the average expected energy losses, and multiple Coulomb scattering in the detector  
 263 material. When at least one muon segment - DT or CSC hits - matches the extrapolated track,  
 264 the corresponding tracker track is indicated as a tracker muon.

265 For low transverse momenta ( $p_T \lesssim 5$  GeV), the tracker muon reconstruction is more efficient  
 266 than the global muon approach. This is due to the fact that tracker muons only require a  
 267 single muon segment in muon system, while the global muon approach requires typically  
 268 segments in at least two muon stations. The global muon approach typically improves the  
 269 tracker reconstruction for  $p_T \gtrsim 200$  GeV.

### 270 2.2.2.2 Solenoid

271 Making use of the knowledge of previous experiments of ALEPH and DELPHI at LEP and H1  
 272 at HERA, CMS choose for a large super conducting solenoid with a length of 12.9 m and  
 273 a inner bore of 5.9 m[23]. With 2 168 turns, a current of 19.5 kA and a total energy of 2.7  
 274 GJ, a large bending power can be obtained for a modestly-sized solenoid. In order to ensure a  
 275 good momentum resolution in the forward regions, a favourable length/radius was necessary.  
 276 In Figure 2.9, a photo of the CMS solenoid is given.

277 The solenoid uses a high-purity aluminium stabilised conductor with indirect cooling from  
 278 liquid helium, together with fully epoxy impregnation. A four-layer winding is implemented that

279 can withstand an outward pressure of 64 atm. The NbTi cable is co-extruded by pure aluminium  
 280 that acts as a thermal stabilizer and has an aluminium alloy for mechanical reinforcement. The  
 281 return of the magnetic field is done by five wheels, noted by YB in [Figure 2.7](#).

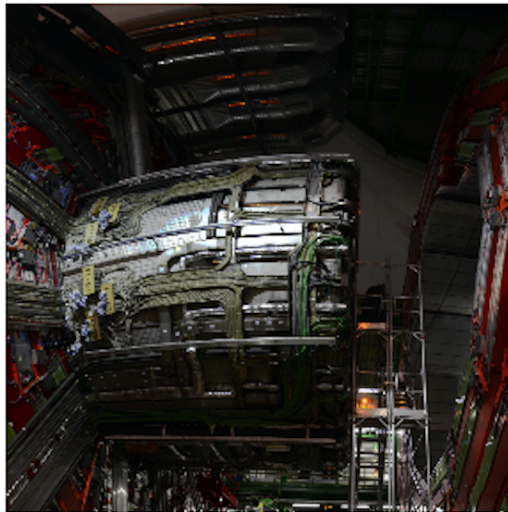


**Figure 2.9:** CMS solenoid during the long shutdown in 2013.

### 282 2.2.2.3 Hadronic calorimeter

283 The hadronic calorimeter (HCAL) is dedicated to precisely measure the energy of charged and  
 284 neutral hadrons via a succession of absorbers and scintillators. This makes it crucial for physics  
 285 analyses with hadronic jets or missing transverse energy. The HCAL extends between 1.77  
 286  $< r < 2.95$  m where  $r$  is the radius in the transverse plane with respect to the beam. Due  
 287 to space limitations, the HCAL needs to be as small as possible and is made from materials  
 288 with short interaction lengths - the length needed for absorbing 36.7% of the hadrons. The  
 289 quality of the energy measurements is dependant on the fraction of the hadronic shower that  
 290 can be detected. Therefore, the HCAL barrel (HB) inside the solenoid is reinforced by an outer  
 291 hadronic calorimeter between the solenoid and muon detectors (HO, see [Figure 2.10](#)), using the  
 292 solenoid as extra absorber. This increases the thickness to 12 interaction lengths. Furthermore,  
 293 it should be as hermetic as possible and extend to large pseudo rapidity values. The HB and HO  
 294 provide measurements for  $|\eta| < 1.3$ , while an end cap on each side (HE,  $1.3 < |\eta| < 3$ ) and a  
 295 forward calorimeter (HF,  $|\eta| < 5.2$ ) extend the pseudo rapidity range.

296 The HB is made of 16 absorber plates where most of them are built from brass and others  
 297 are made from stainless steel and is about five to ten interaction lengths thick. The HE is also  
 298 composed of brass absorber plates and has a thickness corresponding to approximately ten  
 299 interaction lengths. The HF experiences intense particle fluxes with an energy of 760 GeV  
 300 deposited on average in a proton interaction at a center of mass of 14 TeV, compared to 100  
 301 GeV in the rest of the detector. Therefore, these are Cherenkov light detectors made of radiation  
 302 hard quartz fibers. The main causes of such large energy events are high energy muons, cosmic  
 303 particles and charged particles from late showering hadrons. During Run I, it became clear that  
 304 the glass windows of the PMTs had to be replaced which was done during LS1 [33]

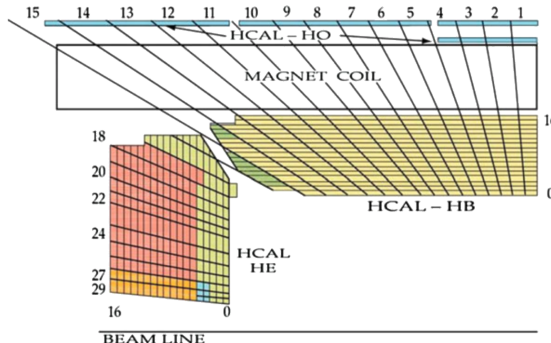


**Figure 2.10:** Tower segmentation for one quarter of the HCAL displayed in the  $rz$  plane[11].

### 305 2.2.2.4 Electromagnetic calorimeter

306 The electromagnetic calorimeter (ECAL) is designed to measure the energy of photons and  
 307 electrons and covers  $|\eta| < 3$ . It is an hermetic, homogeneous detector and consists of 75 848  
 308 lead tungstate ( $\text{PbWO}_4$ ) crystals. These crystals have a fast response time - 80% of the light  
 309 is emitted within 25 ns - and are radiation hard. The electromagnetic showers produced by  
 310 passing electrons or photons ionize the crystal atoms which emit a blue-green scintillation light,  
 311 that is collected by silicon avalanche photodiodes (APDs) in the barrel and vacuum phototriodes  
 312 (VPTs) in the end caps. The crystals and the APD response is sensitive to temperature changes  
 313 and require a stable temperature.

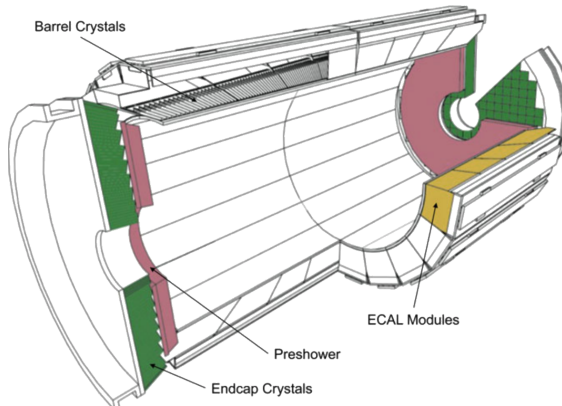


**Figure 2.11:** Schematic cross section of the electromagnetic calorimeter[11].

314 There are three regions: a central barrel (EB), a endcap region (EE) and a preshower (ES)  
 315 (Figure 2.11). The EB has an inner radius of 129 cm and corresponds to a pseudo rapidity  
 316 of  $0 < |\eta| < 1.479$ . At a distance of 314 cm from the vertex and covering a pseudo rapidity  
 317 of  $1.479 < |\eta| < 3.0$ , are the EE. They consist of semi-circular aluminium plates from which  
 318 structural units of  $5 \times 5$  crystals (super crystals) are supported. The ES is placed in front of  
 319 the crystal calorimeter over the end cap pseudo rapidity range with two planes of silicon strip  
 320 detectors as active elements.

The electromagnetic shower will typically involve more than one channel. More than 90% of

the energy of a 35 GeV electron or photon is contained in a  $5 \times 5$  matrix of crystals. Therefore, a clustering algorithm is performed in order to associate the energy deposits to the particles impinging the calorimeter. The achieved precision[34] for the barrel is  $2.10^{-3}$  rad in  $\phi$  and  $10^{-3}$  in  $\eta$ . For the end caps this is  $5.10^{-3}$  rad in  $\phi$  and  $2.10^{-3}$  in  $\eta$ . The energy is reconstructed by a super cluster algorithm, taking into account energy radiated via bremsstrahlung or conversion:

$$E_{e/\gamma} = GF_{e/\gamma} \sum_{i \in \text{cluster}} S_i(t) V C_i A_i, \quad (2.5)$$

where  $G$  is the absolute energy scale in GeV/ADC,  $F$  the energy containment corrections (depends on type of particle, its energy and pseudo rapidity, eg shower leakage and bremsstrahlung losses for electrons),  $S(t)$  the relative channel variation with time,  $C$  the relative channel response and  $A$  the amplitude in ADC counts. The energy resolution is given by

$$\frac{\sigma(E)}{E} = \frac{2.8\%}{\sqrt{E}} \oplus \frac{0.128}{E(\text{GeV})} \oplus 0.3\%, \quad (2.6)$$

321 in the absence of a magnetic field, where the contributions come from the stochastic, noise and  
 322 constant terms respectively. The dominating term is the constant term ( $E_{\text{shower}} \approx 100\text{GeV}$ ) and  
 323 thus the performance is highly dependent on the quality of calibration and monitoring .

324 In Run I, the energy reconstruction happened via a weighted sum of the digitized samples[35].  
 325 For Run II however, the reconstruction had to be made more resistant for out of time pile up  
 326 and a multi-fit approach has been set in to place. In this approach, the pulse shape is modelled  
 327 as a sum of one in-time pulse plus the out of time pulses [34]. The energy resolution is less  
 328 than 2% in the central barrel region and 2-5 % elsewhere.

### 329 2.2.2.5 Inner tracking system and operations

330 The tracking system (tracker) [36] is the detecting unit closest to the point of interaction.  
 331 Responsible for the reconstruction of trajectories from charged particles with  $|\eta| < 2.5$  that are  
 332 bent by the magnetic field, it provides a measurement of the momentum. The tracker is also  
 333 responsible for the determination of the interaction point or vertex. It should be able to provide  
 334 high granularity as well as speed, and be able to endure high radiation. For this reason, the  
 335 CMS collaboration choose silicon detector technology.

336 The tracking system consists of a cylinder of 5.8 m long and 2.5 m in diameter. It is immersed  
 337 in a co-axial magnetic field of 3.8 T due to the solenoid. As shown Figure 2.12, the tracker  
 338 is built up from a large silicon strip tracker with a small silicon pixel inside. The inner region,  
 339 pixel ( $4.4 < r < 10.2$  cm), gets the highest flux of particles. Therefore, pixel silicon sensors  
 340 of  $100 \times 150$   $\mu\text{m}$  area used. It consists of three cylindrical barrels that are complemented by  
 341 two discs of pixel modules at each side. The silicon strip tracker ( $20 < r < 116$  cm ) has three  
 342 subdivisions. The Tracker Inner Barrel and Discs (TIB, TID, see Figure 2.14) are composed  
 343 of four barrel layers accompanied by three discs at each end. The outer part of the tracker -  
 344 Tracker Outer Barrel (TOB) - consists of 6 barrel layers. In the outer discs, there are nine discs  
 345 of silicon sensors, referred to as Tracker End Caps (TEC).

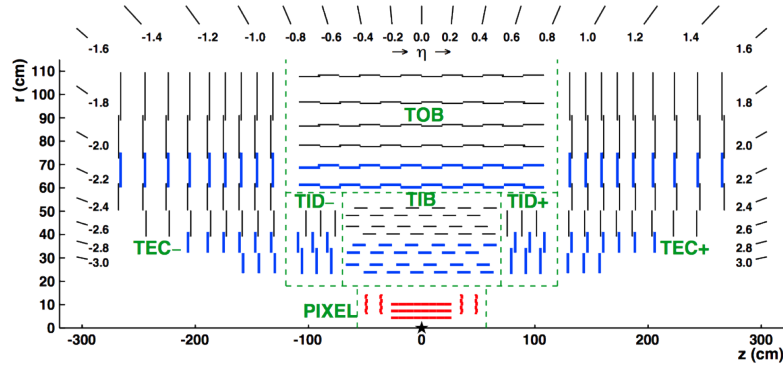


**Figure 2.12:** Schematic cross section of the top half of the CMS tracking system in the  $r$ - $z$  plane. The centre of tracker is shown with a star and corresponds to the approximate position of the proton collision point. The green dashed lines are an indication for each named tracker subsystem. The strip tracker modules that provide two-dimensional hits are shown by thin, black lines, while those able to reconstruct three-dimensional hit positions are shown by thick, blue lines. The pixel modules, shown in red, also provide three-dimensional hits. [22]

346 The pixel, shown in Figure 2.13 has 1440 modules that cover an area of about 1 m<sup>2</sup> and have  
 347 66 million pixels. It provides a three-dimensional position measurement of the hits arising from  
 348 the interaction from charged particles with the sensors. In transverse coordinate ( $r\phi$ ), the hit  
 349 position resolution is about 10  $\mu\text{m}$ , while 20-40  $\mu\text{m}$  is obtained in the longitudinal coordinate  
 350 ( $z$ ). The sensor plane position provides the third coordinate. The silicon strip trackers consists  
 351 of 15 148 single sided modules placed in the TIB, TID and the first four rings of the TEC.  
 352 They provide 9.3 million readout channels. In the TOB and the outer three rings of the TEC,  
 353 double sided modules are used. These modules are constructed from two back-to-back single  
 354 sided modules, where one module is rotated through a stereo angle. This covers an active area  
 355 of about 198 m<sup>2</sup>. The TIB and TID provide position measurements in  $r\phi$  with a resolution  
 356 of approximately 13-38  $\mu\text{m}$ , while the TOB provides a resolution of about 18-47  $\mu\text{m}$ . The  
 357 resolution in the  $z$  direction is approximately 230  $\mu\text{m}$  in the TIB/TID and 530  $\mu\text{m}$  in the TOB.  
 358 To allow overlay and avoid gaps in acceptance, each module is shifted slightly in  $r$  or  $z$  with  
 359 respect to its neighbouring modules within a layer. With this detector lay out, at least nine  
 360 points per charged particle trajectory can be measured in an  $|\eta|$  range up to 2.4.

During the first data taking period of the LHC (2010 to 2013), the tracker operated at +4°C. With the higher LHC beam intensities from 2015 onwards, the tracker needs to be operated at much lower temperatures. This is due to the fact with intense irradiation, the doping concentration changes, the leakage current increases proportional to the fluence and the charge collection efficiency decreases due to charge trapping. Mostly the leakage current ( $I$ ) is affected by the temperature change:

$$I \propto T^2 e^{-\frac{E_g}{2kT}}, \quad (2.7)$$

361 where  $T$  is the operating temperature,  $E_g$  the band gap and  $k$  the Boltzmann constant. There is  
 362 approximately a factor 15 between the leakage currents at room temperatures and at -10 °C.

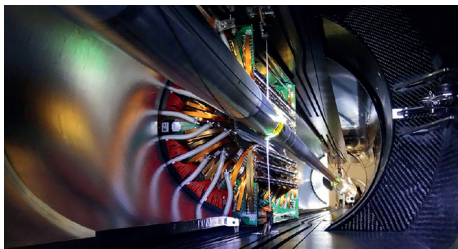


**Figure 2.13:** The pixel barrel being re-installed after the Long Shutdown in 2015, around the beam pipe at CMS[37]

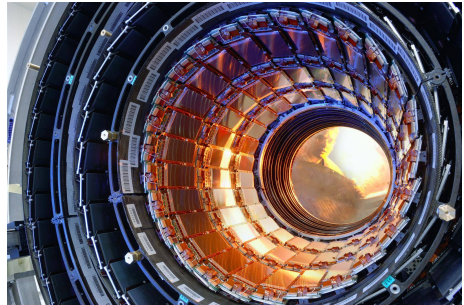


**Figure 2.14:** First half of the inner tracker barrel, consisting of three layers of silicon modules.[38]

363 During the LS1, the CMS cooling plant was refurbished[39](Figure 2.16) and the fluorocarbon  
 364 cooling system overhauled. To help to suppress the humidity inside the tracker, new methods  
 365 for vapour sealing and insulation were applied (Figure 2.15). Furthermore, several hundred  
 366 high-precision sensors are used to monitor the humidity and temperature. In order to get as  
 367 dry air as possible, a new dry-gas plant provides eight times more dry gas (air or nitrogen)  
 368 than during the first run, and allows regulation if the flow. As final addition, the cooling  
 369 bundles outside the tracker are equipped with heater wires and temperature sensors in order to  
 370 maintain safe operations above the cavern dew point For the data taking in 2015-2016, the  
 371 tracker operated at  $-15^{\circ}\text{C}$ .

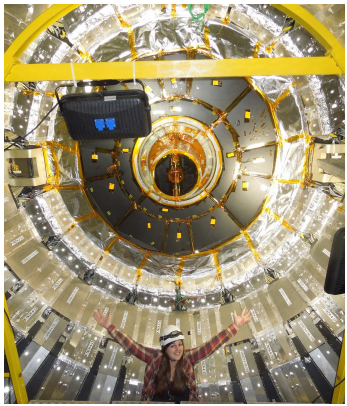


**Figure 2.15:** Tracker bulkhead being put into closed state with insulation pieces installed during an early trial in fall 2013



**Figure 2.16:** New Tracker high-capacity dry-gas plant with membrane separation system[26]

### 372 Track reconstruction

373 An iterative tracking algorithm is responsible for the reconstruction of the tracks made by  
 374 charged particles in the inner tracking system. Each iteration consists of four steps[23]: the  
 375 track-seed generation, the pattern recognition algorithm, removal of track-hit ambiguities and

376 a final track fit.

377 The seed generation is the first step. It consists of finding reconstructed hits that are usable  
 378 for seeding the subsequent track-finding algorithm. They are identified from a group of at  
 379 least three reconstructed hits in the tracker, or from a pair of hits while requiring the origin  
 380 of the track segment to be compatible with the nominal beam-collision point. Since the pixel  
 381 has a higher granularity compared to the strip tracker, its seed generation efficiency is higher.  
 382 The overall efficiency exceeds 99%. The second step of each iteration, the pattern recognition  
 383 algorithm, uses the seeds as a starting point for a Kalman filter method [31, 32]. This algorithm  
 384 extrapolates the seed trajectory towards the next tracker layer taking into account the magnetic  
 385 field and multiple scattering effects. The track parameters are updated when a compatible hit  
 386 in the next layer is found. This procedure continues until the outermost layer is reached. Since  
 387 the Kalman filter method can result in multiple tracks associated to the same seed, or different  
 388 tracks sharing the same hits, a removal of ambiguities is necessary. This ambiguity resolving is  
 389 done by removing tracks that are sharing too many hits from the list of track candidates. The  
 390 tracks with highest number of hits or with the lowest  $\chi^2$  if the track fit is kept. The updated  
 391 track parameters are then refitted using the Kalman filter method, where all hits found in the  
 392 pattern recognition step are taken into account. The fit is done twice - once outwards from the  
 393 beam line towards the calorimeters, and inwards from the outermost track hit to the beam line  
 394 -, improving the estimation of the track parameters.

395 All hits that are unambiguously associated to the final track are removed from the list of  
 396 available hits. In order to associate the remaining hits, the procedure is repeated with looser  
 397 track reconstruction criteria. The use of the iterative track reconstruction procedure has a  
 398 high track finding efficiency, where the fake track reconstruction rate is negligible. For muons,  
 399 this results in a global track reconstruction efficiency exceeding 98%, and 75-98% for charged  
 400 hadrons.

#### 401 Primary vertex reconstruction

402 The primary vertex reconstruction should be able to measure the location of all proton interaction  
 403 vertices in each event: the signal vertex and all vertices from pile up events. It consists of a vertex  
 404 finding and a vertex fitting algorithm and happens in three steps. Tracks are selected to be  
 405 consistent with being produced promptly in the primary interaction by imposing requirements  
 406 on the track parameters[36] By grouping reconstructed tracks according to the z coordinate of  
 407 their closest approach to the beam line, vertices for all interaction in the same beam crossing  
 408 are found, at CMS this is done by a deterministic annealing algorithm [40] . On top of this,  
 409 a vertex fitting algorithm like the Adaptive Vertex fitter [41], is performed. This creates the  
 410 three-dimensional primary-vertex position. With this fit, the contribution from long-lived hadron  
 411 decays is reduced by down weighting the tracks with a larger distance to the vertex. The primary  
 412 vertex corresponding to the highest sum of squared track transverse momenta is noted as the  
 413 point of the main interaction. The resolution on the primary vertex is about 14  $\mu\text{m}$  in  $r\phi$  and  
 414 about 19  $\mu\text{m}$  in the z direction for primary vertices with the sum of the track  $p_T > 100$  GeV  
 415 for 2016 data taking.

416 **2.2.3 Data acquisition**

417 At a design luminosity of  $10^{34} \text{ 1/(m}^2 \text{ s)}$ , the proton interaction rate exceeds 1 GHz. This makes  
 418 it impossible for the CMS experiment to store all the data generated. For this, a two level trigger  
 419 system has been put in place. The first level (Level-1) is a custom hardware system, while a  
 420 second level (HLT) is software based running on a large farm of computers. In run II, with the  
 421 increase in centre of mass energy and a higher luminosity, a larger number of simultaneous  
 422 inelastic collisions per crossing is expected with respect to run I. For this, the CMS Level-1 has  
 423 been upgraded [42].

424 **CMS Level-1 trigger**

425 The Level-1 trigger has to be a flexible, maintainable system, capable of adapting to the evolving  
 426 physics programme of CMS [43]. Its output rate is restricted to 100 kHz imposed by the CMS  
 427 readout electronics. It is implemented by custom hardware and selects events containing candi-  
 428 date objects - eg ionization deposits consistent with a muon, or energy clusters corresponding  
 429 to an electron / photon / tau lepton / missing transverse energy / jet. Collisions with large  
 430 momenta can be selected by using scalar sum of the transverse momenta of the jets.

431 By buffering the raw data from the CMS subdetectors in front-end drivers, the level-1 trigger  
 432 has a pipeline memory of 3.2  $\mu\text{s}$  to decide whether to keep an event or reject it. The trigger  
 433 primitives (TP) from the calorimeters and muon detectors are processed in several steps and  
 434 combined into a global trigger. This information is then combined with the input from the other  
 435 subsystems. The separate inputs are synchronized to each other and the LHC orbit clock and  
 436 sent to the global trigger module. Here, level-1 trigger algorithms are performed within 1  $\mu\text{s}$  to  
 437 decide whether to keep the event.

438 For run II, all hardware, software, databases and the timing control system have been replaced.  
 439 The main changes are that the muon system now uses the redundancy of three muon detector  
 440 system earlier to make a high resolution muon trigger. Other upgrades are that the calorimeter  
 441 system isn't bound any more for streaming data the data and the global trigger has more level-1  
 442 trigger algorithms.

443 **CMS HLT trigger**

444 The HLT is an array of commercially available computers with programmable menu that has  
 445 output rate of on average 400 Hz for off-line event storage. The data processing is based on a  
 446 HLT path. This is a set of algorithmic steps to reconstruct objects and make selections on them.  
 447 Here, the information of all sub detectors can be used to perform algorithms on higher level  
 448 reconstructed objects.

449 **2.2.4 CMS computing model**

450 The selected data is stored, processed and dispersed via the Worldwide Large Hadron Collider  
 451 GRID (WLCG)[44, 45]. This has a tiered structure that function as a single, coherent system:

452 At CERN, a single Tier-0 is located. The raw data collected by CMS is archived here, and  
 453 a first reconstruction of the data is done. This data is then already in a file format usable for

454 physics analysis. Furthermore, it is able to reprocess data when new calibrations are made  
455 available. The Tier-0 site distributes this data to a total of seven Tier-1 centres. They carry out  
456 data reprocessing and store real data as well as simulated data. The Tier-1 further distribute  
457 the data to over 50 Tier-2 centres. These make the data accessible for physics analysis and are  
458 also being used for the production of simulated data. The data is made accessible for physicists  
459 around the world.



# Event generation, simulation and reconstruction

460

3

## 461 3.1 Collision event generation

462 3.1.1 Parton distribution functions and the hard interaction

463 3.1.2 Parton showering

464 3.1.3 Hadronization and decay

465 3.1.4 Underlying event

466 3.1.5 Event reconstruction and identification

## 467 3.2 Detector simulation

## 468 3.3 Physics object reconstruction and identification

469 3.3.1 The particle flow event reconstruction method

470 3.3.2 Identification of particles

471 3.3.2.1 Muon reco and ID

472 3.3.2.2 Electron reco and ID

473 3.3.2.3 Jet reco and ID of b quarks

474 3.3.2.4 Missing transverse energy reconstruction

475 3.3.3 Calibrations and corrections



# The search for FCNC involving a top quark and a Z boson

<sup>476</sup>

4

<sup>477</sup> **4.1 Model assumptions**

<sup>478</sup> **4.2 Data and simulation**

<sup>479</sup> **4.2.1 Standard Model Background simulation**

<sup>480</sup> **4.2.2 FCNC signal simulation**

<sup>481</sup> **4.2.3 Trigger requirements**

<sup>482</sup> **4.3 Baseline event selection**

<sup>483</sup> **4.4 Data driven background estimation**

<sup>484</sup> **4.5 Regions and channels**

<sup>485</sup> **4.6 Construction of template distributions**

<sup>486</sup> **4.7 Systematic uncertainties**

<sup>487</sup> **4.8 Limit setting procedure**

<sup>488</sup> **4.9 Result and discussion**



## Conclusion and outlook

5

---



# Bibliography

---

- 491 [1] R. BARATE et al.: **Search for the standard model Higgs boson at LEP**. In: *Phys. Lett.*,  
492 **B565**: (2003), pp. 61–75. doi: [10.1016/S0370-2693\(03\)00614-2](https://doi.org/10.1016/S0370-2693(03)00614-2). arXiv: [hep-ex/0306033](https://arxiv.org/abs/hep-ex/0306033)  
493 [[hep-ex](#)] (see p. 3).
- 494 [2] KENNETH HERNER: **Higgs Boson Studies at the Tevatron**. In: *Nucl. Part. Phys. Proc.*,  
495 **273-275**: (2016), pp. 852–856. doi: [10.1016/j.nuclphysbps.2015.09.131](https://doi.org/10.1016/j.nuclphysbps.2015.09.131) (see p. 3).
- 496 [3] ABDELHAK DJOUADI: **The Anatomy of electro-weak symmetry breaking. I: The Higgs  
497 boson in the standard model**. In: *Phys. Rept.*, **457**: (2008), pp. 1–216. doi: [10.1016/j.physrep.2007.10.004](https://doi.org/10.1016/j.physrep.2007.10.004). arXiv: [hep-ph/0503172](https://arxiv.org/abs/hep-ph/0503172) [[hep-ph](#)] (see p. 3).
- 498 [4] SERGUEI CHATRCHYAN et al.: **Observation of a new boson at a mass of 125 GeV with  
499 the CMS experiment at the LHC**. In: *Phys. Lett.*, **B716**: (2012), pp. 30–61. doi:  
500 [10.1016/j.physletb.2012.08.021](https://doi.org/10.1016/j.physletb.2012.08.021). arXiv: [1207.7235](https://arxiv.org/abs/1207.7235) [[hep-ex](#)] (see p. 3).
- 501 [5] GEORGES AAD et al.: **Observation of a new particle in the search for the Standard  
502 Model Higgs boson with the ATLAS detector at the LHC**. In: *Phys. Lett.*, **B716**:  
503 (2012), pp. 1–29. doi: [10.1016/j.physletb.2012.08.020](https://doi.org/10.1016/j.physletb.2012.08.020). arXiv: [1207.7214](https://arxiv.org/abs/1207.7214) [[hep-ex](#)]  
504 (see p. 3).
- 505 [6] LYNDON EVANS and PHILIP BRYANT: **LHC Machine**. In: *Journal of Instrumentation*, **3**:08  
506 (2008), S08001. URL: <http://stacks.iop.org/1748-0221/3/i=08/a=S08001> (see p. 3).
- 507 [7] THOMAS SVEN PETTERSSON and P LEFÈVRE: **The Large Hadron Collider: conceptual  
508 design**. Tech. rep. CERN-AC-95-05-LHC. Oct. 1995, p. 20 and 22. URL: <https://cds.cern.ch/record/291782> (see p. 3).
- 509 [8] JORG WENNINGER and EZIO TODESCO: **Large Hadron Collider momentum calibration  
510 and accuracy**. Tech. rep. CERN-ACC-2017-0007. Geneva: CERN, Feb. 2017. URL:  
511 <https://cds.cern.ch/record/2254678> (see p. 4).
- 512 [9] CINZIA DE MELIS: **The CERN accelerator complex. Complexe des accélérateurs du  
513 CERN**. In: (July 2016). General Photo. URL: <https://cds.cern.ch/record/2197559> (see  
514 p. 4).
- 515 [10] G. AAD et al.: **The ATLAS Experiment at the CERN Large Hadron Collider**. In: *JINST*,  
516 **3**: (2008), S08003. doi: [10.1088/1748-0221/3/08/S08003](https://doi.org/10.1088/1748-0221/3/08/S08003) (see p. 4).
- 517 [11] S. CHATRCHYAN et al.: **The CMS Experiment at the CERN LHC**. In: *JINST*, **3**: (2008),  
518 S08004. doi: [10.1088/1748-0221/3/08/S08004](https://doi.org/10.1088/1748-0221/3/08/S08004) (see pp. 4, 13).
- 519

- 521 [12] K. AAMODT et al.: **The ALICE experiment at the CERN LHC.** In: *JINST*, **3**: (2008),  
 522 S08002. doi: [10.1088/1748-0221/3/08/S08002](https://doi.org/10.1088/1748-0221/3/08/S08002) (see p. 4).
- 523 [13] A. AUGUSTO ALVES JR. et al.: **The LHCb Detector at the LHC.** In: *JINST*, **3**: (2008),  
 524 S08005. doi: [10.1088/1748-0221/3/08/S08005](https://doi.org/10.1088/1748-0221/3/08/S08005) (see p. 4).
- 525 [14] M. BONGI et al.: **Astroparticle physics at LHC: The LHCf experiment ready for data  
 526 taking.** In: *Nucl. Instrum. Meth.*, **A612**: (2010), pp. 451–454. doi: [10.1016/j.nima.2009.08.039](https://doi.org/10.1016/j.nima.2009.08.039) (see p. 4).
- 528 [15] G. ANELLI et al.: **The TOTEM experiment at the CERN Large Hadron Collider.** In:  
 529 *JINST*, **3**: (2008), S08007. doi: [10.1088/1748-0221/3/08/S08007](https://doi.org/10.1088/1748-0221/3/08/S08007) (see p. 4).
- 530 [16] B. ACHARYA et al.: **The Physics Programme Of The MoEDAL Experiment At The LHC.**  
 531 In: *Int. J. Mod. Phys.*, **A29**: (2014), p. 1430050. doi: [10.1142/S0217751X14300506](https://doi.org/10.1142/S0217751X14300506).  
 532 arXiv: [1405.7662 \[hep-ph\]](https://arxiv.org/abs/1405.7662) (see p. 5).
- 533 [17] BY JAMES GILLIES: **Luminosity? Why don't we just say collision rate?** In: (Mar. 2011).  
 534 URL: <http://cds.cern.ch/record/1997001> (see p. 5).
- 535 [18] BY HARRIET JARLETT and HARRIET KIM JARLETT: **LHC pushes limits of performance.**  
 536 In: (Aug. 2016). URL: <http://cds.cern.ch/record/2212301> (see p. 5).
- 537 [19] OLIVER SIM BRÜNING, PAUL COLLIER, P LEBRUN, et al.: **LHC Design Report.** CERN Yellow  
 538 Reports: Monographs. Geneva: CERN, 2004. URL: <https://cds.cern.ch/record/782076>  
 539 (see p. 5).
- 540 [20] JEAN-LUC CARON: **Cross section of LHC dipole.. Dipole LHC: coupe transversale.**  
 541 AC Collection. Legacy of AC. Pictures from 1992 to 2002. May 1998. URL: <https://cds.cern.ch/record/841539> (see p. 6).
- 543 [21] **Technical proposal.** LHC Tech. Proposal. Cover title : CMS, the Compact Muon Solenoid  
 544 : technical proposal. Geneva: CERN, 1994. URL: <https://cds.cern.ch/record/290969>  
 545 (see p. 7).
- 546 [22] G. L. BAYATIAN et al.: **CMS physics: Technical design report.** In: (2006) (see pp. 7,  
 547 15).
- 548 [23] G L BAYATIAN, S CHATRCHYAN, G HMAYAKYAN, et al.: **CMS Physics: Technical Design  
 549 Report Volume 1: Detector Performance and Software.** Technical Design Report CMS.  
 550 There is an error on cover due to a technical problem for some items. Geneva: CERN,  
 551 2006. URL: <https://cds.cern.ch/record/922757> (see pp. 7, 11, 16).
- 552 [24] BY CIAN O'LUANAIGH: **LHC progresses towards higher intensities.** In: (Aug. 2015).  
 553 URL: <http://cds.cern.ch/record/2051986> (see p. 7).
- 554 [25] CMS COLLABORATION: **Detector Drawings.** CMS Collection. Mar. 2012. URL: <https://cds.cern.ch/record/1433717> (see p. 8).
- 556 [26] BY CORINNE PRALAVORIO and CORINNE PRALAVORIO: **Major work to ready the LHC  
 557 experiments for Run 2.** In: (May 2015). URL: <http://cds.cern.ch/record/2024977>  
 558 (see pp. 7, 16).
- 559 [27] S CHATRCHYAN, V KHACHATRYAN, A M SIRUNYAN, et al.: **Performance of the CMS Drift  
 560 Tube Chambers with Cosmic Rays.** In: *J. Instrum.*, **5**:arXiv:0911.4855. CMS-CFT-  
 561 09-012 (Nov. 2009), T03015 . 47 p. URL: <http://cds.cern.ch/record/1223944> (see  
 562 pp. 9–10).

- 563 [28] LUIGI GUIDUCCI: **CMS muon system towards LHC Run 2 and beyond**. Tech. rep. CMS-  
 564 CR-2014-333. Geneva: CERN, Oct. 2014. URL: <https://cds.cern.ch/record/1966038>  
 565 (see p. 10).
- 566 [29] CARLO BATTILANA: **The CMS muon system status and upgrades for LHC run-2 and**  
 567 **performance of muon reconstruction with 13 TeV data**. Tech. rep. CMS-CR-2016-  
 568 437. Geneva: CERN, Dec. 2016. URL: <http://cds.cern.ch/record/2239185> (see  
 569 p. 10).
- 570 [30] SERGUEI CHATRCHYAN et al.: **Performance of CMS muon reconstruction in  $pp$  col-**  
 571 **lision events at  $\sqrt{s} = 7$  TeV**. In: *JINST*, 7: (2012), P10002. DOI: <10.1088/1748-0221/7/10/P10002>. arXiv: [1206.4071 \[physics.ins-det\]](1206.4071) (see p. 11).
- 573 [31] R. FRÜHWIRTH: **Application of Kalman filtering to track and vertex fitting**. In: *Nu-*  
 574 *clear Instruments and Methods in Physics Research Section A: Accelerators, Spectrom-*  
 575 *eters, Detectors and Associated Equipment*, 262:2 (1987), pp. 444–450. DOI: [http://dx.doi.org/10.1016/0168-9002\(87\)90887-4](http://dx.doi.org/10.1016/0168-9002(87)90887-4) (see pp. 11, 17).
- 577 [32] PIERRE BILLOIR: **Progressive track recognition with a Kalman like fitting procedure**.  
 578 In: *Comput. Phys. Commun.*, 57: (1989), pp. 390–394. DOI: [10.1016/0010-4655\(89\)90249-X](10.1016/0010-4655(89)90249-X) (see pp. 11, 17).
- 580 [33] EMRAH TIRAS, BURAK BILKI, and YASAR ONEL: **Commissioning of CMS Forward Hadron**  
 581 **Calorimeters with Upgraded Multi-anode PMTs and μTCA Readout**. In: (2016).  
 582 arXiv: [1611.05232 \[physics.ins-det\]](1611.05232) (see p. 12).
- 583 [34] L. BRIANZA: **Precision crystal calorimetry in LHC Run II with the CMS ECAL**. In:  
 584 *Journal of Instrumentation*, 12:01 (2017), p. C01069. URL: <http://stacks.iop.org/1748-0221/12/i=01/a=C01069> (see p. 14).
- 586 [35] SERGUEI CHATRCHYAN et al.: **Energy Calibration and Resolution of the CMS Elec-**  
 587 **tromagnetic Calorimeter in  $pp$  Collisions at  $\sqrt{s} = 7$  TeV**. In: *JINST*, 8: (2013).  
 588 [*JINST8,9009(2013)*], P09009. DOI: <10.1088/1748-0221/8/09/P09009>. arXiv: <1306.2016>  
 589 [*hep-ex*] (see p. 14).
- 590 [36] SERGUEI CHATRCHYAN, VARDAN KHACHATRYAN, ALBERT M SIRUNYAN, et al.: **Description**  
 591 **and performance of track and primary-vertex reconstruction with the CMS tracker**.  
 592 In: *J. Instrum.*, 9:arXiv:1405.6569. CERN-PH-EP-2014-070. CMS-TRK-11-001 (May  
 593 2014). Comments: Replaced with published version. Added journal reference and DOI,  
 594 P10009. 80 p. URL: <http://cds.cern.ch/record/1704291> (see pp. 14, 17).
- 595 [37] BY CHRISTINE SUTTON: **Chronicles of CMS: the saga of LS1**. In: (May 2015). URL:  
 596 <http://cds.cern.ch/record/2024986> (see p. 16).
- 597 [38] **A beautiful barrel for CMS**. In: (Mar. 2014). URL: <http://cds.cern.ch/record/1998635> (see p. 16).
- 599 [39] **Cool running for CMS tracker**. In: (Mar. 2014). URL: <http://cds.cern.ch/record/1998606> (see p. 16).
- 601 [40] K. ROSE: **Deterministic annealing for clustering, compression, classification, re-**  
 602 **gression, and related optimization problems**. In: *Proceedings of the IEEE*, 86:11 (Nov.  
 603 1998), pp. 2210–2239. DOI: <10.1109/5.726788> (see p. 17).

- 604 [41] WOLFGANG WALTENBERGER: **Adaptive Vertex Reconstruction**. Tech. rep. CMS-NOTE-  
605 2008-033. Geneva: CERN, July 2008. URL: <https://cds.cern.ch/record/1166320> (see  
606 p. 17).
- 607 [42] L. CADAMURO: **The CMS Level-1 trigger system for LHC Run II**. In: *Journal of Instrumentation*, **12**:03 (2017), p. C03021. URL: <http://stacks.iop.org/1748-0221/12/i=03/a=C03021> (see p. 18).
- 610 [43] VARDAN KHACHATRYAN et al.: **The CMS trigger system**. In: *JINST*, **12**:01 (2017),  
611 P01020. doi: [10.1088/1748-0221/12/01/P01020](https://doi.org/10.1088/1748-0221/12/01/P01020). arXiv: [1609.02366](https://arxiv.org/abs/1609.02366) [physics.ins-det]  
612 (see p. 18).
- 613 [44] CLAUDIO GRANDI, DAVID STICKLAND, LUCAS TAYLOR, ACHILLE PETRILLI, and ALAIN HERVÉ:  
614 **CMS Computing Model: The "CMS Computing Model RTAG"**. Tech. rep. CMS-NOTE-  
615 2004-031. CERN-LHCC-2004-035. LHCC-G-083. Geneva: CERN, Dec. 2004. URL:  
616 <http://cds.cern.ch/record/814248> (see p. 18).
- 617 [45] CHRISTOPH ECK, J KNOBLOCH, LESLIE ROBERTSON, et al.: **LHC computing Grid: Technical  
618 Design Report. Version 1.06 (20 Jun 2005)**. Technical Design Report LCG. Geneva:  
619 CERN, 2005. URL: <https://cds.cern.ch/record/840543> (see p. 18).